Dual bandgap operation of a GaAs/Si photoelectrode

Mekan Piriyev, Gabriel Loget, Yoan Léger, Lipin Chen, Antoine Létoublon, Tony Rohel, Christophe Levallois, Julie Le Pouliquen, Bruno Fabre, Nicolas Bertru, et al.

Dual bandgap operation of a GaAs/Si photoelectrode

Mekan Piriyev[a], Gabriel Loget[b], Yoan Léger[a], Lipin Chen[a, 1], Antoine Létoublon[a], Tony Rohel[a], Christophe Levallois[a], Julie Le Pouliquen[a], Bruno Fabre[b], Nicolas Bertru[a,], Charles Cornet[a,*].*

[a]*Univ Rennes, INSA Rennes, CNRS, Institut FOTON – UMR 6082, F-35000Rennes, France*

[b]*Univ Rennes, CNRS, ISCR (Institut des Sciences Chimiques de Rennes) – UMR6226, F-35000 Rennes, France*

Corresponding authors: charles.cornet@insa-rennes.fr, nicolas.bertru@insa-rennes.fr

[1] Tianjin Key Laboratory of Film, Electronic and Communication Devices, School of Integrated Circuit Science and Engineering, Tianjin, University of Technology, Tianjin 300384, China

ABSTRACT: The development of high-efficiency photoelectrodes at low manufacturing cost is of great interest for the production of renewable and green hydrogen through solar-driven water splitting. In this work, we use structural, optical, and photoelectrochemical characterizations to study the performance of unprotected epitaxial GaAs/Si photoelectrodes during photocorrosion. More specifically, we demonstrate that photoanodes including 1-µm thick GaAs epitaxially grown thin film on a low-cost Si substrate can produce a higher photocurrent than those measured for expensive commercial GaAs wafers. Based on photoelectrochemical experiments under monochromatic excitation, we show that the improved photocurrent has to be related to the dual-bandgap operation of the GaAs/Si photoelectrode, benefiting from both GaAs and Si photo-generated carriers. This result opens new possibilities to further design efficient and low-cost dual-bandgap photoelectrodes.

KEYWORDS: GaAs/Si photoelectrode, dual bandgap, photoelectrochemical cell, light absorption, III-V semiconductors on silicon

1. Introduction

The need for green, clean energy to face the global demand while avoiding CO_2 emissions placed the quest for sustainable energy production and storage as one of the most challenging topic in research. [1–3] Hydrogen can be employed as an efficient energy vector due to its large storage capacity (142 MJ/kg) with zero CO_2 emissions. [4] Presently, several processes are known for hydrogen production such as steam reforming, electrolysis and biomass conversion.[4] Nevertheless, the production of hydrogen from renewable sources at more affordable costs remains challenging. Solar water splitting via photoelectrochemical (PEC) cells is considered as one of the promising routes for hydrogen generation, in which semiconductor photoelectrodes are used to perform the cathodic hydrogen evolution reaction (HER) and the anodic oxygen evolution reaction (OER) from the two most abundant resources: sun and water. [5,6] The semiconductor materials to be used as photoelectrodes, their intrinsic physico-chemical properties and their fabrication processes are crucial for the device to have both, the highest efficiency and also the lowest hydrogen production cost [7,8] Thus, the ideal photoelectrode material should combine simultaneously (*i*) a large light absorption with solar energy harvesting capabilities over the largest spectral range as possible, (*ii*) a bandgap and band lineups appropriate to drive the water splitting half-reactions at lower overpotential, (*iii*) a longer lifetime of operation and (*iv*) low fabrication costs, for instance through the choice of Earth-abundant materials. III-V semiconductors show a great potential for solar water splitting due to remarkable intrinsic physical properties leading to large light absorption and enhanced mobility for charge carriers and efficient charge transfers to the electrolyte, thus leading to high photocurrent densities and large solar-to-hydrogen (STH) efficiencies. [7,9] As a result, relatively high-efficiency photoelectrodes were achieved with III-V semiconductors, as compared to oxide

semiconductors or traditional silicon. [7,10] In addition, alloying of III-V materials (through the fine control of the alloys composition) enables tailoring of the bandgap energy and band lineups between the photoelectrode and the electrolyte. The nature of the bandgap (indirect or direct) can be adjusted as well through alloying, to enhance solar energy harvesting capabilities. [11] Despite the excellent optical properties of III-V semiconductors, their poor stability (against corrosion) in aqueous electrolytes was pointed out in the pioneering work of Khalesev and Turner, showing nevertheless promising photocurrent densities of 10.1 mA/cm^2 with a $Pt/GaInP_2/GaAs$ photoelectrode under 1-sun illumination. [12] This issue was recently fixed by Hu *et al.* who have investigated thin-film materials, especially metal-oxide layers as a protection for III-V photoelectrodes.[13] They successfully demonstrated an n/p^+ GaAs-based photoanode operating at a photocurrent density of 14.3 mA/cm^2 with a stable operation for more than 25h thanks to a TiO_2 passivation layer and an optically transparent Ni OER co-catalyst.[14] This proposed passivation method was further confirmed for a $GaP_{1-x}Sb_x$ photoanode, indicating that this approach can be transposed to a large variety of other III-V materials.[15] To increase the junction voltage of III-V photoelectrodes, III-V multijunctions architectures composed of series-associated p-n junctions can be fabricated using complex processes, with multiple doping steps and necessary tunnel junctions. The development of these III-V technologies occurs at the expense of high substrate and fabrication costs and sustainability issues with the use of toxic materials or critical resources for their production. [16]

Most research works dealing with III-V photoelectrodes were carried out using commercial binary III-V substrates, [7,10] that are approximately ten times more expensive than silicon substrates. [8] This fact motivated the development of III-V thin films or nanostructures photoelectrodes on Si.[17–19] More recently, planar III-V nitrides photoelectrodes on silicon

substrate were employed by Nötzel et al., who reported a photocurrent density of 13.6 mA/cm^2 at 1.23 V vs RHE, which was further improved by using surface quantum dots activated structures.[20] Simultaneously, the first planar Zinc-Blende III-V photoelectrode grown on a silicon substrate was demonstrated with GaPSb alloy, producing a photocurrent density of 10 mA/cm^2 at 1.23 V vs RHE, and with subsequent protection against corrosion. [15] This work was further extended to other unprotected III-V/Si materials systems, i.e., GaP and GaAsP alloy grown on Si with the measured photocurrent densities equal to 1.0 and 11.3 mA/cm^2, respectively. [21] But still, in these various demonstrations, the Si substrate was considered as a starting template for further photo-active III-V material regrowth, the performance of which is usually governed by the crystal defects density generated during III-V/Si heteroepitaxy.[22] Despite the advantages of using the III-V/Si association as a dual-bandgap architecture discussed in reference [19], the spectral contribution of the Si substrate itself to the photoresponse of a planar III-V/Si photoelectrode has never been reported so far. Note that in this study, the "dual-bandgap" simply refers to the association of two different materials with two different bandgaps, and "dual bandgap operation" means that the carriers photo-generated in both layers can contribute to the electrochemical reaction, without the needs of any p-n junction in the semiconductor. It is thus fundamentally different from the conventional multi-junction tandem architecture.

In this work, we study the self-oxidation operation of a GaAs/Si:n photoelectrode. Based on structural, optical, photoelectrochemical characterizations, and comparison with a bare GaAs photoelectrode, we specifically analyze the corrosion-induced photocurrent performance of the III-V photoelectrode grown on the low-cost Si substrate. Photoelectrochemical characterization under monochromatic excitation is used to confirm that the large corrosion photocurrent

measured with a GaAs/Si photoanode originates from the dual-bandgap operation of the electrode. Comparison of these photocurrents allows to assess photoanodic performance that could ultimately be reached in a water splitting system with adequate protection and catalyst layers. The interest of using such a simple dual-bandgap architecture as a single photoelectrode is finally discussed.

2. Experimental section

Samples of study. A non-intentionally doped (nid) GaAs thin film (1-μm thick) in a bi-domain configuration was grown by Molecular Beam Epitaxy (MBE) on an n-doped silicon (Si:n) substrate (350 μm) (see details in the Supplementary Data). In addition, a homoepitaxial nid GaAs (1 μm) was grown on an n-doped GaAs (350 μm) for comparison of photoelectrochemical properties. A commercial n-doped GaAs wafer (350 μm), was used as a reference material to compare the structural and optical properties as well as photoelectrochemical performances.

Photoelectrode preparation. Photoanodes (PA) from the epitaxial GaAs/Si, GaAs/GaAs samples and the GaAs wafer were prepared by cleaning the sample in the ultrasound cleaner for 10s and subsequently dried with N_2 gas. The backside was slightly scratched and Ohmic contact was made using Gallium-Indium eutectic (99.99%, Alfa Aesar) and silver paste (Electron Microscopy Sciences). The electrochemically active surface area was defined using an epoxy resin (EA 3423, Henkel from Loctite) covering the backside and the edges of the PA. The characterization methods and corresponding additional figures are described in details in the Supporting Information.

3. Results and discussion

3.1 Structural characterization

The structural characterizations of the epitaxially grown GaAs (1 µm)/Si:n and the reference GaAs:n wafer (350 µm) were first carried out using X-Ray Diffraction (XRD) in the conventional ω/2θ mode. Figure 1 (a) shows XRD ω/2θ scans performed in the vicinity of the Si (004). A thin Bragg peak is first observed at 69.13° for the GaAs/Si sample, corresponding to the Si substrate. A well-defined Bragg peak is also observed at a 2θ angle (66.02°) for the epitaxial GaAs/Si, very close to the position of the commercial GaAs wafer peak (66.06°), both giving a mean lattice constant of 0.565 ± 0.002 nm corresponding to the lattice constant of the bulk GaAs. [23]

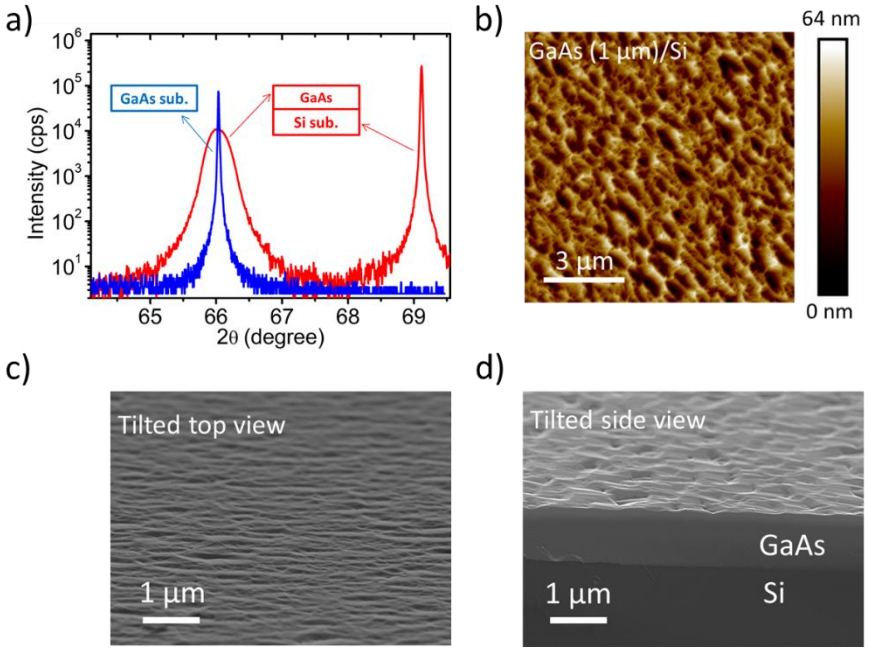

Figure 1. Structural characterizations of the epitaxial GaAs(1 µm)/Si:n sample and the GaAs:n (350 µm) wafer. (a) XRD ω/2θ scan performed in the vicinity of the Si(004) Bragg peak for GaAs/Si (red) and GaAs (blue); (b) Atomic force microscopy image of GaAs/Si surface morphology with a rms roughness of 9.2 nm; (c-d) Scanning electron microscopy tilted top and side view images of GaAs/Si.

However, in these profiles, the 350 µm GaAs wafer Bragg peak appears narrow with an integral breadth (IB) of 0.018°, comparable to the Si one and resolution-limited. In contrast, the Bragg peak associated to the 1 µm GaAs layer in the GaAs/Si sample (IB of 0.294°) is much

broader than what is expected for a good quality layer with the same thickness (expected IB of 0.043°). From the peak position and reciprocal space mapping (Figure S1, Supplementary Data) it is clear that (*i*) the GaAs grown on the Si substrate is fully relaxed (and consequently its intrinsic physical properties can be compared directly to the bare GaAs wafer) and that (*ii*) GaAs/Si has a large density of crystal defects (induced by the relaxation process or the polar-on-non-polar epitaxy), namely micro-twins, misfit dislocations and antiphase boundaries. [22] These crystal defects are expected in bi-domain and mismatched III-V/Si samples when no strategies are used to bury or annihilate them. [24,25] To further investigate sample morphology, tapping mode atomic force microscopy (AFM) and scanning electron microscopy (SEM) were performed. The 10 x 10 μm² AFM image of the GaAs/Si sample is given in Figure 1 (b). An AFM image at the same scale for the GaAs wafer is reported in Figure S2 for comparison. Epitaxial GaAs/Si sample surface reveals a root-mean-square (rms) roughness of 9.2 nm, higher than the one measured for the GaAs wafer (0.7 nm). This indicates the presence of numerous crystal defects in the GaAs epilayer grown on Si. [24] Figure 1 (c-d) show the tilted-top and side view SEM images for the epitaxial GaAs/Si sample. SEM image at the same scale is given for the GaAs wafer in Figure S3 for comparison. The Si substrate and the 1-μm thick GaAs epilayer can be easily distinguished from the two different contrasts observed in Figure 1 (d). Roughness of the epitaxial GaAs/Si sample surface is thus confirmed over a scale larger than the AFM one.

3.2 Photoelectrochemical characterization

Note that the presence of numerous crystal defects and roughness were considered for years as device killers in the field of III-V/Si photonics or photovoltaics. [26,27] Especially, these defects are usually considered as non-radiative recombination centers, hampering efficient transport in photoelectric devices. Thus, relatively lower photoelectrochemical (PEC)

performance (in terms of photocurrent density and quantum efficiency) would be expected for the epitaxial GaAs/Si sample, as compared to the almost defect-free commercial GaAs wafer. In order to examine PEC properties, photoanodes (PA) of the epitaxial GaAs/Si, GaAs/GaAs and GaAs wafer were prepared (details in 2. Experimental section). The PEC measurements were carried out using a three-electrode setup in 0.2 M H_2SO_4 electrolyte (measured pH=0.35). The net photocurrent density (j_{net}) was determined from the difference between photocurrent density of the electrode under 1-sun illumination (AM 1.5G, 100 mW cm^{-2}) and under dark conditions ($j_{net} = j_{light} - j_{dark}$, see Figure S4) for the GaAs/Si PA, GaAs/GaAs PA as well as GaAs PA, and represented as a function of the applied potential vs the reversible hydrogen electrode potential (RHE) in Figure 2 (a)**.** Note that the results presented below will be discussed in terms of measured photocurrent at 1.23V vs. RHE, a standard condition usually considered for water splitting applications, although the photocurrent measured in this study originates from photocorrosion. Surprisingly, a slightly (but significantly) higher photocurrent at 1.23 V is obtained for the GaAs/Si PA (j_{net} = 13.74 mA/cm^2) than for the GaAs PA (j_{net} = 12.22 mA/cm^2). A similarly shaped *j*-V curve was obtained for the epitaxial GaAs/GaAs photoanode (PA) when compared to the epitaxial GaAs/Si:n PA. Importantly, the observed j_{net} at 1.23 V vs. RHE for the GaAs/GaAs PA (7.94 mA/cm^2) is significantly smaller than the GaAs/Si:n PA, which can be related to the amount of charge carriers photogenerated and successfully transported to the electrolyte.

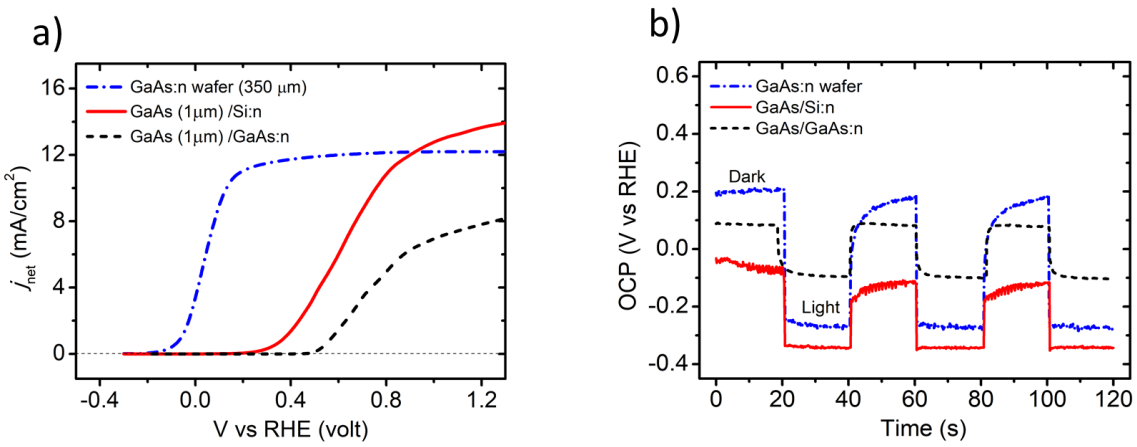

Figure 2. a) Net photocurrent density vs voltage (j_{net} - V) and b) open-circuit potential (OCP) measurements for the photoanodes of GaAs:n wafer (350 μm), epitaxial GaAs(1 μm)/ Si:n and epitaxial GaAs(1 μm)/ GaAs:n in 0.2 M H_2SO_4 electrolyte (measured pH=0.35) under simulated AM 1.5G illumination

This result indicates that the sample with the largest density of defects also generates the highest photocurrent which seems, at first, contradictory with previous reports using III-V/Si for photonics or photovoltaics. One can expect that, GaAs/Si will lead to a depletion width that extends much further into the bulk because of its targeted nid low-doping level. Therefore, the electric field in the GaAs/Si would lead to enhanced carrier collection and thus higher photocurrent obscuring other loss channels. However, the recombination occurs not only in the bulk, but also in the depletion layer at the surface states and interfacial defects. [28] Nevertheless, in the absence of recombinations in the depletion layer, only the minority carriers generated within the distance of diffusion length (L_p) can be separated efficiently and transferred through the interface for redox reaction. [29,30] L_p is in the range of 0.1 – 0.9 μm for GaAs (<1 μm, thickness of the epilayer), therefore, carriers collection should be limited firstly by the diffusion length and secondly by the width of depletion layer. The Mott Schottky analysis for GaAs/Si was performed (Figure S6 (a), in supplementary file) and the apparent doping density for GaAs/Si is found to be 7.25×10^{17} cm^{-3}. The observed high-doping density likely results from

the presence of antiphase boundaries in the material, which are electrically active and act as donor defects. [21] The width of the depletion layer as a function of the doping density is calculated using the data extracted from Mott Schottky analysis and plotted in Figure S6 (b). It appears to be that, the width of the depletion layer does not extend into the bulk in GaAs/Si and is below than the thickness of the epilayer. The high photocurrent of GaAs/Si suggests that (*i*) carriers transport in photoelectrodes is not affected by the crystal defects in the same way as in photonic or photovoltaic devices, [21] and (*ii*) there are additional contributions to the photocurrent, beyond the GaAs one, yielding higher photocurrent, which will be discussed in the following.

Additionally, onset potentials (V_{onset}) of 0.38 V, 0.48 V and -0.08 V are extracted for GaAs/Si, GaAs/GaAs and GaAs, respectively, showing that the onset potential is significantly larger for both, GaAs/Si PA and GaAs/GaAs PA when benchmarked to GaAs wafer PA. The delay in V_{onset} can be attributed to the influence of interfaces. In the case of the GaAs/GaAs PA, impurities can remain at the interface between the epilayer and the substrate giving rise to interfacial states. The onset potential and the slope are convoluted with kinetics of the electrochemical reaction. As no catalyst was used in this study, the slopes of *j*-V curves are compared relatively and estimated to be 0.028, 0.016 and 0.049 Siemens/cm^2 for GaAs/Si, GaAs/GaAs and GaAs PA, respectively. Note that, GaAs/Si (GaAs/GaAs) is an epitaxial stack of nid GaAs and n-type Si substrate (n-type GaAs substrate), and thus does not involve multiple p-n junctions. Therefore, an increase in photovoltage (V_{ph}) or decrease in onset potential (V_{onset}) is not expected for the epitaxial samples.

Open circuit potential (OCP) measurements were carried out in the same three-electrode cell at the equilibrium to investigate the influence of the light on the studied samples, as shown

in Figure 2 (b). Photopotential (V_{ph}) was then inferred from the difference between OCP measured in light and dark ($V_{ph} = OCP_{light} - OCP_{dark}$). A lower V_{ph} is obtained for the epitaxial GaAs/Si (0.22 ± 0.05 V), GaAs/GaAs (0.18 ± 0.02 V) than for the GaAs (0.45 ± 0.03 V), confirming that the GaAs/Si PA requires a higher applied external voltage to enable photoelectrochemical charge transfer. This is consistent with the larger V_{onset} measured for the epitaxial GaAs/Si PA, and is related to the presence of additional interfaces in the case of GaAs/Si (Si/GaAs/electrolyte) and GaAs/GaAs (GaAs/GaAs/electrolyte) that may lead to potential drop at the hetero-interface.

It is worth mentioning that, without any protective layer, epitaxial GaAs/Si, GaAs/ GaAs and GaAs wafer PA are not expected to drive Oxygen Evolution Reaction (OER). Measured photocurrents originate from III-V photocorrosion which is already highlighted in references [15,31–33] Nevertheless, this does not change the main conclusions of the present work, as photocorrosion is a redox reaction taking place as a result of photo-induced charge generation and transportation. For this reason, the large photocurrent detected with the GaAs/Si PA is intriguing and potentially of great interest for water splitting applications, and a deeper analysis of the light absorption and photogeneration of the charge carriers in the studied PA is proposed in the following.

3.3 Optical characterization

Spectroscopic ellipsometry measurements were used to characterize the optical constants of the GaAs epilayer and in particular its light absorption deduced from the imaginary part of the optical index. The optical constants were measured at room temperature in the photon energy range of 0.6 – 4.2 eV and subsequently fitted with Tauc-Lorentz model to calculate the

absorption coefficient (α). The extracted absorption spectra, given in Figure S8, indicate that light absorption lies within the same order of magnitude for both GaAs/Si and GaAs wafer, and therefore that crystal defects do not affect significantly carrier photogeneration in GaAs. From absorption coefficient measurements, and neglecting electron-hole recombination and charge carriers diffusion length, it becomes possible to evaluate the maximum theoretical photocurrent density ($j_{\text{theoretical}}$) generated in the two PA. For comparison, this calculation is first performed by considering only the epitaxial GaAs thin layer (1 µm) and the commercial GaAs wafer (350 µm) as photoactive layers. In this regard, the fraction of the photon flux absorbed by each GaAs layer in both samples ($\Phi_{sample(\lambda)}$) is calculated from its thickness (d_{sample}), its absorption coefficient ($\alpha_{sample(\lambda)}$), and the spectral photon flux of the simulated solar AM 1.5G ($\Phi_{0(\lambda)}$) using the equation below [3]:

$$\Phi_{sample}(\lambda) = \Phi_0(\lambda) \times \left[1 - \exp\left(-\alpha_{sample}(\lambda) \times d_{sample}\right)\right]$$

Figure 3 (a) superimposes the solar spectral photon flux $\Phi_0(\lambda)$ and absorbed photon flux $\Phi(\lambda)$ for a 1µm-thick GaAs layer (green solid line) and the 350 µm-thick commercial GaAs wafer (blue solid line).

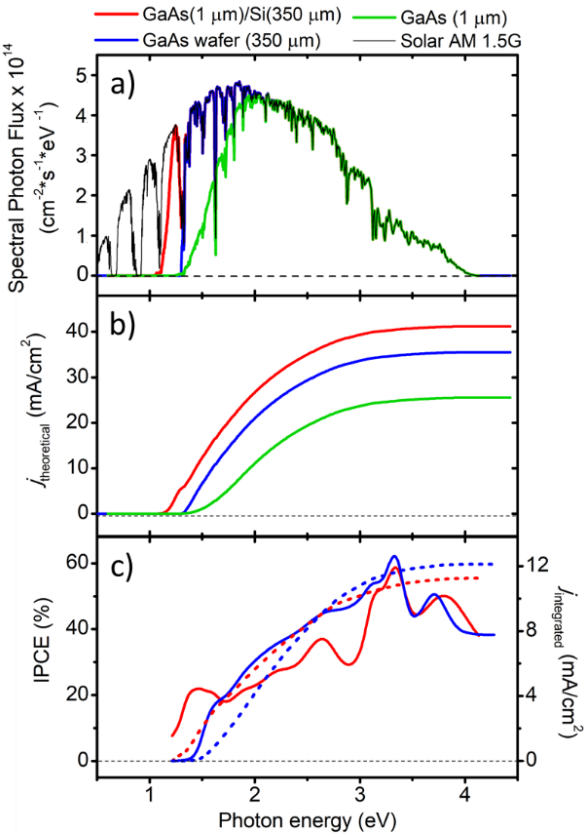

Figure 3. a) Fraction of the photons absorbed by GaAs from the spectral photon flux of the AM 1.5G solar spectrum (black) for the 350-μm thick GaAs wafer (blue), 1-μm thick GaAs layer (green) and 1-μm thick GaAs epitaxial layer grown on 350-μm thick Si substrate (red); b) $j_{theoretical}$ (mA/cm^2) calculated neglecting e^-/h^+ recombination; c) Incident photon-to-current efficiency (IPCE) measured in the energy range of (1.21 - 4.13) eV at 0.8 V vs RHE . Right axis presents the integrated photocurrents $j_{integrated}$ (short-dashed lines) extracted from IPCE data.

Assuming that each photon absorbed generates one electron/hole pair, the total number of the absorbed photons multiplied by the electric charge (q) gives the maximum current density that can be produced. Figure 3 (b) shows the deduced maximum integrated current density $j_{\text{theoretical}}$ for the epitaxial 1-μm GaAs layer as the green solid line (commercial 350 μm GaAs wafer as the blue solid line) with a photocurrent density at saturation equal to 25.5 mA/cm^2 (35.2 mA/cm^2), in close agreement with that calculated in references [3,10]. The difference in photocurrent densities between the two configurations is thus mostly related to the difference of GaAs

thicknesses considered (1 μm vs 350 μm), the impact of which is enhanced when the absorption is lower (at energies near the GaAs bandgap)

3.4 Quantum efficiency

Then, the incident photon-to-current conversion efficiency (IPCE) was measured for the epitaxial GaAs/Si and GaAs PA using a tunable wavelength light-emitting diode (LED) illumination source with the external applied potential at 0.8 V vs RHE. Figure 3 (c) shows the IPCE curve and the integrated photocurrent density ($j_{\text{integrated}}$) plot extracted from IPCE data for the GaAs/Si and GaAs where a maximum of IPCE around 60% was observed for both PA. The $j_{\text{integrated}}$ at saturation was estimated to be 11 mA/cm^2 and 12 mA/cm^2 for GaAs/Si and GaAs, respectively, showing a good consistency of the measurements with the j - V voltammetric curves. As expected, the GaAs PA has a zero IPCE (no photoresponse) in the photon energy below 1.42 eV which corresponds to the bandgap of GaAs. [23] Whereas, this is not the case for the GaAs/Si that has a non-zero IPCE value below 1.42 eV. This sub-bandgap photoresponse could be mainly due to the Si substrate contribution to the photocurrent. A more quantitative picture can be given through additional measurements of the photocurrent under specific wavelength monochromatic excitation.

3.5 Photocurrent density with a tunable monochromatic light source

The photocurrent density at 0.8 V vs RHE was measured with monochromatic light source (LED) at three different excitation energies (E_{exc}). The spectral information of each source is reported in Table S1 in the Supplementary Data. The first E_{exc} (1.89 eV) was set to a photon energy significantly larger than the bandgap of GaAs. The second E_{exc} (1.36 eV) was set to a photon energy just below the bandgap of GaAs and the third one (1.23 eV) was chosen to lie

significantly below the bandgap of GaAs. All the E_{exc} are however larger than the Si bandgap (1.12 eV). Figure 4 (a) displays the photocurrent density measured alternatively at different E_{exc} and in dark conditions for the reference GaAs PA, showing a photocurrent density of 0.56 mA/cm^2 measured at E_{exc} = 1.89 eV. For the E_{exc} smaller than the band gap of GaAs (1.42 eV), it can be observed that the reference GaAs PA is not responding as the photocurrent is close to zero. In contrast to the reference GaAs, the epitaxial GaAs/Si PA results in a smaller but significant net photocurrent density equal to 0.12 mA/cm^2 and 0.07 mA/cm^2 even at smaller E_{exc} energies (1.36 and 1.23 eV) than the bandgap of GaAs (Figure 4(b)).

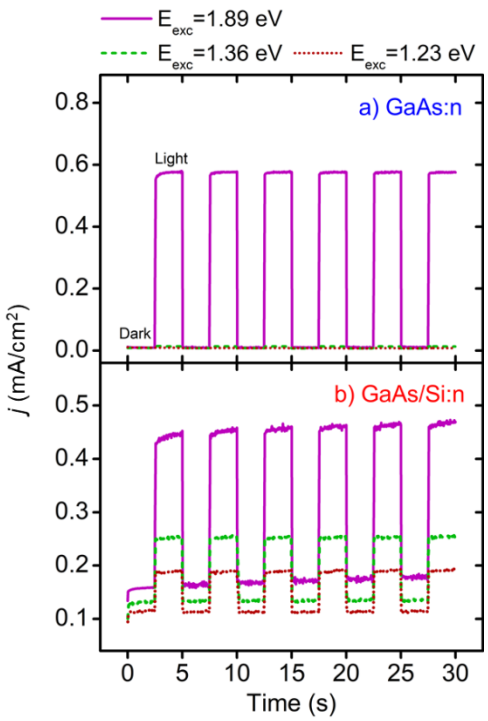

Figure 4. Photocurrent density measured under E_{exc} of 1.89 eV (purple solid line), 1.36 eV (green dashed line) and 1.23 eV (brown dotted line) for (a) GaAs:n PA and (b) GaAs/Si:n PA at 0.8 V vs RHE. The average spectral width and power of the LED light source are detailed in Table S1.

These experiments show unambiguously that the Si substrate is photoactive in the GaAs/Si PA. To further clarify the PEC performance of GaAs/Si, a photoactive 350 µm-thick Si layer was

added to the model for the determination of the absorbed photon flux and the maximum possible photocurrent density $j_{theoretical}$ generated. Results are shown by red curves in Figure 3(a-b). From these calculations, one can easily observe that the addition of Si as a photoactive material allows the absorption of the solar photon flux at lower energy (Figure 3 (a)), resulting in photocurrent starting at lower energy, and reaching a higher saturation value of 41.1 mA/cm^2 (Figure 3(b)).

This therefore explains why the photocurrent reached with GaAs/Si PA is higher than the one measured with the reference GaAs PA, and gives the hope to reach even improved performances for single photoelectrodes with such dual bandgap configuration and, without any complex p-n architecture. These results also highlight that carriers photogenerated in the Si material are surprisingly able to cross the GaAs/Si interface, and the whole GaAs layer despite the hetero-interface band offsets and the GaAs crystal defects. Interestingly, the photocurrent density of bare n-type Si substrate PA without GaAs epitaxial layer is in the range of 0.1 mA/cm^2, which is attributed to the presence of insulating SiO_x native oxide. Following the dipping of the bare n-type Si photoanode into HF (10%) for 2 min to remove SiO_x from the surface, the photocurrent density is increased twice reaching ~0.2 mA/cm^2 (Figure S5). This value is in the same order of magnitude as the one measured under monochromatic conditions with the GaAs/Si PA, which additionally strengthens the previous observation. Here, it is interesting to note that the photoactivity of Si is not systematically observed for other III-V materials grown on Si substrates when such a dual bandgap architecture is considered for photo-electrochemistry. Similar analysis was performed on GaP/Si and GaP PA (Figure S9). Again, these PA are not designed with any p-n junctions, neither with doping engineering nor with controlled intermixing at the hetero-interface. In this case, the IPCE for both epitaxial GaP/Si and GaP PA increases massively above 2.7 eV (direct bandgap of GaP) and shows a close to zero

value below that energy indicating that Si substrate does not contribute to the PEC activity of the GaP/Si PA. We attribute this difference between the two materials systems to the relative positioning of the III-V semiconductor bands and their band lineup with the bands of Si, which are different (Figure S10). Indeed, as the valence band (VB) of Si is well aligned with the VB of GaAs [34], the minority charge carriers, i.e., the photogenerated holes, can be easily transferred from Si to GaAs. Therefore, the amount of the effective charges used in oxidation process increases which consequently results in an enhancement of the photocurrent. In the case of GaP/Si, the VB maximum of Si is significantly higher than that of GaP, thus it will impose an energy barrier for the transfer of the photogenerated holes from Si to GaP. Consequently, the development of efficient dual-bandgap III-V/Si single photoelectrodes is conditioned by the choice of an appropriate III-V semiconductor, which band lineups with Si are favorable to promote photoelectrochemical charge transfer.

4. Conclusions

In conclusion, we have demonstrated the dual-bandgap operation of a photoelectrode composed of a thin 1 µm-thick GaAs epilayer grown on the low-cost Si substrate. We especially show that despite crystal defects and additional band offsets, the GaAs/Si dual-bandgap photoanode allows reaching higher light-limited net corrosion-induced photocurrents than those obtained with photoelectrodes fabricated from commercial defect-free bare 350 µm-thick GaAs substrates. The participation of carriers photogenerated in the Si substrate is found to be the origin of enhanced photocurrent. This demonstration, obtained with a simple material design, opens prospects for the development of high-efficiency dual-bandgap III-V/Si photoelectrodes with adapted protective and catalytic layers, for solar hydrogen production.

CRediT authorship contribution statement

Mekan Piriyev: XRD, AFM and PEC characterization and data analysis, ellipsometry measurements and data analysis, analysis of light absorption properties. Wrote and finalized original draft. **Gabriel Loget:** PEC measurements and data analysis. **Yoan Léger:** analysis of results and discussion, analysis of the light absorption properties. **Lipin Chen:** PEC measurements and data analysis. **Antoine Létoublon:** XRD measurements and data analysis. **Tony Rohel:** designed and fabricated the samples. **Christophe Levallois:** ellipsometry measurements and data analysis. **Julie Le Pouliquen:** SEM measurements. **Bruno Fabre:** analysis of PEC results. **Nicolas Bertru:** conceived the idea, designed and fabricated the samples, analysis of results, wrote and finalized the manuscript. **Charles Cornet:** conceived the idea, designed and fabricated the samples, analysis of results, wrote and finalized the manuscript. All authors reviewed and commented on the manuscript.

Declaration of competing interest

The authors declare that they have no known competing financial interests or personal relationships that could have appeared to influence the work reported in this paper**.**

Acknowledgements

The authors acknowledge RENATECH (French Network of Major Technology Centers) within Nanorennes for technological support, V. Demange and C. Derouet for access to XRD Osirix platform (ScanMAT, UAR 2025 University of Rennes 1-CNRS). This research was supported by Rennes Métropole through the “REMOTE” project and the “France 2030” French

National Research Agency NAUTILUS Project (Grant no. ANR-22-PEHY-0013). Lipin Chen acknowledges the China Scholarship Council (CSC) for her PhD financial support (No. 2017-6254).

Appendix A. Supplementary data

The Supplementary data contains additional figures and tables and detailed description of the materials and sample preparation methods: silicon substrate preparation; epitaxial growth of GaAs; characterization techniques: X-Ray Diffraction (XRD); Atomic Force Microscopy (AFM); Scanning Electron Microscopy (SEM); Photoelectrochemical (PEC) measurements; Open Circuit Potential (OCP); Spectroscopic ellipsometry; Spectral photon flux and $j_{\text{theoretical}}$; Incident photon-to-current conversion efficiency (IPCE); Measurement of the photocurrent density with a tunable monochromatic light source.

REFERENCES

[1] N.S. Lewis, D.G. Nocera, Powering the planet: Chemical challenges in solar energy utilization, PNAS. 103 (2006) 15729–15735. https://doi.org/10.1073/pnas.0603395103.

[2] K. Rajeshwar, R. McConnell, S. Licht, eds., Solar Hydrogen Generation: Toward a Renewable Energy Future, Springer-Verlag, New York, 2008. https://doi.org/10.1007/978-0-387-72810-0.

[3] Z. Chen, T.F. Jaramillo, T.G. Deutsch, A. Kleiman-Shwarsctein, A.J. Forman, N. Gaillard, R. Garland, K. Takanabe, C. Heske, M. Sunkara, E.W. McFarland, K. Domen, E.L. Miller, J.A. Turner, H.N. Dinh, Accelerating materials development for photoelectrochemical hydrogen production: Standards for methods, definitions, and reporting protocols, Journal of Materials Research. 25 (2010) 3–16. https://doi.org/10.1557/JMR.2010.0020.

[4] M. Steinberg, H.C. Cheng, Modern and prospective technologies for hydrogen production from fossil fuels, International Journal of Hydrogen Energy. 14 (1989) 797–820. https://doi.org/10.1016/0360-3199(89)90018-9.

[5] M. Grätzel, Photoelectrochemical cells, Nature. 414 (2001) 338–344. https://doi.org/10.1038/35104607.

[6] F. Decker, S. Cattarin, PHOTOELECTROCHEMICAL CELLS | Overview, in: J. Garche (Ed.), Encyclopedia of Electrochemical Power Sources, Elsevier, Amsterdam, 2009: pp. 1–9. https://doi.org/10.1016/B978-044452745-5.00035-6.

[7] J. Tournet, Y. Lee, S.K. Karuturi, H.H. Tan, C. Jagadish, III–V Semiconductor Materials for Solar Hydrogen Production: Status and Prospects, ACS Energy Lett. 5 (2020) 611–622. https://doi.org/10.1021/acsenergylett.9b02582.
[8] M.R. Shaner, H.A. Atwater, N.S. Lewis, E.W. McFarland, A comparative technoeconomic analysis of renewable hydrogen production using solar energy, Energy Environ. Sci. 9 (2016) 2354–2371. https://doi.org/10.1039/C5EE02573G.
[9] T. Yao, X. An, H. Han, J.Q. Chen, C. Li, Photoelectrocatalytic Materials for Solar Water Splitting, Advanced Energy Materials. 8 (2018) 1800210. https://doi.org/10.1002/aenm.201800210.
[10] J.H. Kim, D. Hansora, P. Sharma, J.-W. Jang, J.S. Lee, Toward practical solar hydrogen production – an artificial photosynthetic leaf-to-farm challenge, Chem. Soc. Rev. 48 (2019) 1908–1971. https://doi.org/10.1039/C8CS00699G.
[11] I. Vurgaftman, J.R. Meyer, L.R. Ram-Mohan, Band parameters for III-V compound semiconductors and their alloys, Journal of Applied Physics. 89 (2001) 5815–5875. https://doi.org/10.1063/1.1368156.
[12] O. Khaselev, J.A. Turner, A Monolithic Photovoltaic-Photoelectrochemical Device for Hydrogen Production via Water Splitting, Science. 280 (1998) 425–427. https://doi.org/10.1126/science.280.5362.425.
[13] S. Hu, N.S. Lewis, J.W. Ager, J. Yang, J.R. McKone, N.C. Strandwitz, Thin-Film Materials for the Protection of Semiconducting Photoelectrodes in Solar-Fuel Generators, J. Phys. Chem. C. 119 (2015) 24201–24228. https://doi.org/10.1021/acs.jpcc.5b05976.
[14] S. Hu, M.R. Shaner, J.A. Beardslee, M. Lichterman, B.S. Brunschwig, N.S. Lewis, Amorphous TiO2 coatings stabilize Si, GaAs, and GaP photoanodes for efficient water oxidation, Science. 344 (2014) 1005–1009. https://doi.org/10.1126/science.1251428.
[15] M. Alqahtani, S. Sathasivam, L. Chen, P. Jurczak, R. Piron, C. Levallois, A. Létoublon, Y. Léger, S. Boyer-Richard, N. Bertru, J.-M. Jancu, C. Cornet, J. Wu, I.P. Parkin, Photoelectrochemical water oxidation of GaP1−xSbx with a direct band gap of 1.65 eV for full spectrum solar energy harvesting, Sustainable Energy Fuels. 3 (2019) 1720–1729. https://doi.org/10.1039/C9SE00113A.
[16] C.F. Blanco, S. Cucurachi, F. Dimroth, J.B. Guinée, W.J.G.M. Peijnenburg, M.G. Vijver, Environmental impacts of III–V/silicon photovoltaics: life cycle assessment and guidance for sustainable manufacturing, Energy Environ. Sci. 13 (2020) 4280–4290. https://doi.org/10.1039/D0EE01039A.
[17] I. Lucci, S. Charbonnier, M. Vallet, P. Turban, Y. Léger, T. Rohel, N. Bertru, A. Létoublon, J.-B. Rodriguez, L. Cerutti, E. Tournié, A. Ponchet, G. Patriarche, L. Pedesseau, C. Cornet, A Stress-Free and Textured GaP Template on Silicon for Solar Water Splitting, Advanced Functional Materials. 28 (2018) 1801585. https://doi.org/10.1002/adfm.201801585.
[18] O. Supplie, M.M. May, H. Stange, C. Höhn, H.-J. Lewerenz, T. Hannappel, Materials for light-induced water splitting: In situ controlled surface preparation of GaPN epilayers grown lattice-matched on Si(100), Journal of Applied Physics. 115 (2014) 113509. https://doi.org/10.1063/1.4869121.
[19] L. Chen, M. Alqahtani, C. Levallois, A. Létoublon, J. Stervinou, R. Piron, S. Boyer-Richard, J.-M. Jancu, T. Rohel, R. Bernard, Y. Léger, N. Bertru, J. Wu, I.P. Parkin, C. Cornet, Assessment of GaPSb/Si tandem material association properties for photoelectrochemical cells, Solar Energy Materials and Solar Cells. 221 (2021) 110888. https://doi.org/10.1016/j.solmat.2020.110888.

[20] P. Kumar, P. Devi, R. Jain, S.M. Shivaprasad, R.K. Sinha, G. Zhou, R. Nötzel, Quantum dot activated indium gallium nitride on silicon as photoanode for solar hydrogen generation, Commun Chem. 2 (2019) 1–7. https://doi.org/10.1038/s42004-018-0105-0.
[21] L. Chen, Y. Léger, G. Loget, M. Piriyev, I. Jadli, S. Tricot, T. Rohel, R. Bernard, A. Beck, J. Le Pouliquen, P. Turban, P. Schieffer, C. Levallois, B. Fabre, L. Pedesseau, J. Even, N. Bertru, C. Cornet, Epitaxial III–V/Si Vertical Heterostructures with Hybrid 2D-Semimetal/Semiconductor Ambipolar and Photoactive Properties, Advanced Science. (n.d.) 2101661. https://doi.org/10.1002/advs.202101661.
[22] I. Lucci, S. Charbonnier, L. Pedesseau, M. Vallet, L. Cerutti, J.-B. Rodriguez, E. Tournié, R. Bernard, A. Létoublon, N. Bertru, A. Le Corre, S. Rennesson, F. Semond, G. Patriarche, L. Largeau, P. Turban, A. Ponchet, C. Cornet, Universal description of III-V/Si epitaxial growth processes, Phys. Rev. Materials. 2 (2018) 060401. https://doi.org/10.1103/PhysRevMaterials.2.060401.
[23] J.S. Blakemore, Semiconducting and other major properties of gallium arsenide, Journal of Applied Physics. 53 (1982) R123–R181. https://doi.org/10.1063/1.331665.
[24] C. Cornet, S. Charbonnier, I. Lucci, L. Chen, A. Létoublon, A. Alvarez, K. Tavernier, T. Rohel, R. Bernard, J.-B. Rodriguez, L. Cerutti, E. Tournié, Y. Léger, M. Bahri, G. Patriarche, L. Largeau, A. Ponchet, P. Turban, N. Bertru, Zinc-blende group III-V/group IV epitaxy: Importance of the miscut, Phys. Rev. Materials. 4 (2020) 053401. https://doi.org/10.1103/PhysRevMaterials.4.053401.
[25] M. Rio Calvo, J.-B. Rodriguez, C. Cornet, L. Cerutti, M. Ramonda, A. Trampert, G. Patriarche, É. Tournié, Crystal Phase Control during Epitaxial Hybridization of III-V Semiconductors with Silicon, Advanced Electronic Materials. 8 (n.d.) 2100777. https://doi.org/10.1002/aelm.202100777.
[26] J.-H. Yang, L. Shi, L.-W. Wang, S.-H. Wei, Non-Radiative Carrier Recombination Enhanced by Two-Level Process: A First-Principles Study, Sci. Rep. 6 (2016) 21712. https://doi.org/10.1038/srep21712.
[27] H. Das, S. Sunkari, H. Naas, Classification of Killer and Non-Killer Silicon Carbide Epitaxial Defects and Accurate Prediction of Device Yield, ECS Trans. 80 (2017) 239. https://doi.org/10.1149/08007.0239ecst.
[28] J.E. Thorne, J.-W. Jang, E.Y. Liu, D. Wang, Understanding the origin of photoelectrode performance enhancement by probing surface kinetics, Chem. Sci. 7 (2016) 3347–3354. https://doi.org/10.1039/C5SC04519C.
[29] L.M. Peter, K.G.U. Wijayantha, A.A. Tahir, Kinetics of light-driven oxygen evolution at α-Fe2O3 electrodes, Faraday Discuss. 155 (2012) 309–322. https://doi.org/10.1039/C1FD00079A.
[30] T. Yao, X. An, H. Han, J.Q. Chen, C. Li, Photoelectrocatalytic Materials for Solar Water Splitting, Advanced Energy Materials. 8 (2018) 1800210. https://doi.org/10.1002/aenm.201800210.
[31] H. Gerischer, On the stability of semiconductor electrodes against photodecomposition, Journal of Electroanalytical Chemistry and Interfacial Electrochemistry. 82 (1977) 133–143. https://doi.org/10.1016/S0022-0728(77)80253-2.
[32] S. Hu, N.S. Lewis, J.W. Ager, J. Yang, J.R. McKone, N.C. Strandwitz, Thin-Film Materials for the Protection of Semiconducting Photoelectrodes in Solar-Fuel Generators, J. Phys. Chem. C. 119 (2015) 24201–24228. https://doi.org/10.1021/acs.jpcc.5b05976.

[33] S. Pishgar, M.C. Mulvehill, S. Gulati, G.U. Sumanasekera, J.M. Spurgeon, Investigation of n-GaAs Photoanode Corrosion in Acidic Media with Various Thin Ir Cocatalyst Layers, ACS Appl. Energy Mater. 4 (2021) 10799–10809. https://doi.org/10.1021/acsaem.1c01768.
[34] C.G. Van de Walle, J. Neugebauer, Universal alignment of hydrogen levels in semiconductors, insulators and solutions, Nature. 423 (2003) 626–628. https://doi.org/10.1038/nature01665.

TOC figure:

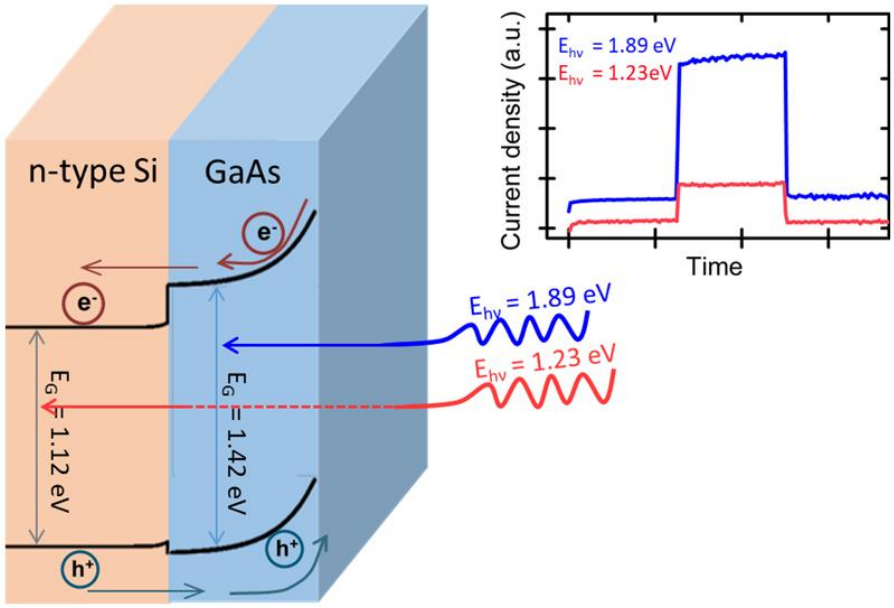

TOC caption: A dual bandgap photoelectrode operation is demonstrated with GaAs thin films grown on Si. The III-V/Si photoelectrode is able to generate a larger photocurrent than a

conventional photoelectrode made of a commercial GaAs substrate, due to the fact that de Si is photoactive.